CARDIFF UNIVERSITY
PRIFYSGOL CAERDYDD

ORCA – Online Research @ Cardiff

This is an Open Access document downloaded from ORCA, Cardiff University's institutional repository:https://orca.cardiff.ac.uk/id/eprint/153067/

This is the author's version of a work that was submitted to / accepted for publication.

Citation for final published version:

Yu, Wenhui, Lee, Jeong Geun, Joo, Young-Hee, Hou, Bo , Um, Doo-Seung and Kim, Chang-Il 2022. Etching characteristics and surface properties of fluorine-doped tin oxide thin films under CF4-based plasma treatment. Applied Physics A: Materials Science and Processing 128 (10) , 942. 10.1007/s00339-022-06082-y

Publishers page: http://dx.doi.org/10.1007/s00339-022-06082-y

Please note:
Changes made as a result of publishing processes such as copy-editing, formatting and page numbers may not be reflected in this version. For the definitive version of this publication, please refer to the published source. You are advised to consult the publisher's version if you wish to cite this paper.

This version is being made available in accordance with publisher policies. See http://orca.cf.ac.uk/policies.html for usage policies. Copyright and moral rights for publications made available in ORCA are retained by the copyright holders.

Etching Characteristics and Surface Properties of Fluorine-doped Tin Oxide Thin Films under CF_4-based Plasma Treatment

Wenhui Yu[1], Jeong Geun Lee[1], Young-Hee Joo[1], Bo Hou[2], Doo-Seung Um[3,†], and Chang-Il Kim[1,†]

[1]School of Electrical and Electronics Engineering, Chung-Ang University, Seoul 06974, Republic of Korea

[2]School of Physics and Astronomy, Cardiff University, Cardiff CF24 3AA, Wales, United Kingdom

[3]Department of Electrical Engineering, Sejong University, Seoul 05006, Republic of Korea

[†]Correspondence: dsum@sejong.ac.kr (D.-S.U.); cikim@cau.ac.kr (C.-I.K.)

Abstract

Owing to their low-cost, high-temperature processability, and excellent optoelectronic properties, fluorine-doped tin oxide (FTO) films are widely used as transparent conductive materials to replace indium-tin-oxide films. Dry etching is increasingly preferred for the patterning of FTO films considering the high-resolution patterning process required for microdevice applications. This study investigates the dry etching of FTO thin films using CF_4-based plasma treatment and analyzes the changes in the etching characteristics and surface properties based on various conditions. The highest etching rate was observed under pure CF_4 conditions, indicating that the chemical etching effect is the primary mechanism during the etching process. Based on the X-ray photoelectron spectroscopy and optical emission spectroscopy results, we determined that the etching of the FTO thin film was caused by the CF_X radical in the CF_4-based plasma. Additionally, the X-ray diffraction results indicate that the plasma etching increased the crystal defects in the FTO film. The etching process smoothened the surface morphology of the FTO film, and the transmittance and bandgap energy were slightly changed as a function of the etching conditions. Additionally, the resistivity of the FTO film improved slightly. The obtained results can benefit the development of high-performance optical devices that use FTO as transparent electrodes.

Keywords: Fluorine-doped tin oxide film, CF_4-based plasma, Etching mechanism, Crystal defect, Surface and physical property

1 Introduction

Transparent conductive oxide (TCO) films are extensively used in various optical devices, such as touch panel displays [1], smart windows [2], indoor solar cells [3], and light-emitting diodes [4], owing to their high transmittance and conductivity in the visible region [5]. To date, indium-tin-oxide (ITO) is the most extensively utilized TCO owing to its high conductivity and optical transmittance [6]. However, ITO is currently restricted in its advancement in optoelectronic technologies because of economic disadvantages and technological obstacles. The limited and scattered distribution of indium in the earth's crust results in high manufacturing costs and an unstable ITO supply. Furthermore, they exhibit poor chemical and mechanical stability and produce metallic indium on the surface after annealing in a reducing atmosphere, thus limiting the device fabrication [7]. Therefore, a stable and widely available transparent conductive material is required to replace ITO [8]. Several materials and processing techniques have been proposed in recent years, including SnO_2-based film systems [9], ZnO-based film systems [10], carbon nanotube films [11], graphene films [12], metallic nanowire networks [13], and metal chalcogenide films [14]. Fluorine-doped SnO_2 (FTO) is the most preferred alternative for ITO owing to its low cost, excellent transmittance and conductivity, chemical stability in acidic and alkaline solutions, high thermal stability, and adequate mechanical properties [15].

The fabrication of microelectrodes for various optoelectronic devices requires the fine patterning of TCO films, and etching is the most commonly used process [16]. Several etching methods have been proposed for FTO films, including wet etching in acidic solutions, electrochemical etching, and laser etching. The wet and electrochemical etching processes are completed in a chemical solution, which results in poor controllability and isotropic etching; therefore, they are unsuitable for high-precision patterning processes [17-19]. Conversely, the laser etching method causes defects such as poor-quality grooves and cracks on the FTO film surface and substrate, which severely affect the optoelectronic performance and durability of the electrodes [20-22]. Therefore, the need for anisotropic etching properties and high uniformity has rendered the dry etching process using plasma the preferred choice for the high-resolution patterning of TCO films. Plasma processing is known to cause various changes in the surface and physical properties of TCO films. Chowdhury et al. used inductively coupled plasma etching with Cl_2/Ar gas to create pyramidal texture patterns on FTO electrodes, which increased the total transmittance owing to the reduced light reflection by the pyramidal pattern [23]. Chantarat et al. reported that the SnO_2 can be reduced to metallic Sn and suboxide of Sn (SnO) on FTO films under an atmosphere of H_2 plasma [24]. Tang et al. reported that oxygen plasma treatment can modulate the energy levels of FTO films. Implanting the oxygen ion in the FTO thin film surface via oxygen plasma treatment reduces the number of oxygen vacancies, which in turn reduces the surface carrier concentration, causing the Fermi level to shift to the valence band and increasing the work function [25].

In addition, it has also been reported that the pretreatment of FTO glass substrates with CF_4 plasma is beneficial to improve the adhesion of subsequent film depositions [26]. However, very limited information is available on the effects of fluorine-based plasmas on FTO films (eg, etch performance and etch mechanism, etc.). Therefore, it is necessary to study the changes in CF_4 plasma etching process in detail.

This study investigated the etching characteristics of FTO films under CF_4-based plasma treatment and analyzed the changes in the surface and physical properties of FTO films after the etching process. The etching process was performed in the high-density plasma system and the highest etching rate was obtained under pure CF_4 plasma conditions. The changes in the crystal structure and chemical composition of the FTO films after plasma etching were confirmed by X-ray photoelectron spectroscopy (XPS) and X-ray diffraction (XRD). The changes in the surface morphology and surface free energy were observed using atomic force microscopy (AFM), field emission scanning electron microscopy (FE-SEM), and contact angle analysis. Additionally, the physical properties, such as optical bandgap and electric mobility, were measured and calculated using ultraviolet–visible light (UV–vis) spectrometer and Hall-effect measurement. These results can form the basis for the development of high-performance optical devices.

2 Experimental Details

A 600-nm-FTO thin film on a soda-lime glass substrate (NSG TEC7, 10 mm × 10 mm) was supplied by the Pilkington Technology Centre (Pilkington Group Ltd.). Before the etching process, the FTO glass was sonicated in isopropyl alcohol, rinsed in deionized (DI) water, and dried using a nitrogen gun to obtain a clean surface.

Etching experiments were performed in a high-density plasma (HDP) system (APTC Selex 200), which combines the benefits of a capacitively coupled plasma and an inductively coupled plasma coil to generate higher plasma densities (Fig. S1). The system was composed of multi-spiral coils and a bushing, with the coil antenna placed above a thick horizontal ceramic window. To generate plasma and control the plasma density, a 13.56-MHz-radio frequency (RF) generator was connected to the plasma antenna. Additionally, a 2-MHz-RF generator was connected to the electrostatic chuck to control the ion flux in the plasma by adjusting the bias voltage. The vacuum in the main process chamber was maintained at 8×10^{-4} Torr, which was achieved using rotary and turbomolecular pumps. The temperature of the substrate can be controlled using an external cooling cycle [27]. In this study, the etching trends of the FTO thin films under CF_4/Ar-mixed plasma were obtained under the following

conditions: total gas flow rate of 100 sccm, RF source power of 500 W, RF bias power of 150 W, process pressure of 15 mTorr, and the substrate was maintained at 25 °C.

The etching rates of the FTO thin films were determined using a depth profiler (α-step 500, KLA Tencor). The behavior of plasma radicals and ions in the chamber during the etching process was characterized using optical emission spectroscopy (OES, VT500, Prime solution). Additionally, modifications in the crystal structure and chemical composition of the films after etching were analyzed using XRD (D8 DISCOVER, Bruker) and XPS (Nexsa, Thermo Fisher Scientific Inc.), respectively. The changes in the surface morphology and roughness of the films were investigated using AFM (NX-10, Park Systems) and FE-SEM (Sigma 300, Carl ZEISS). The contact angles were obtained using the solidified drop method with a contact angle analyzer (Phoenix 300, SEO). Furthermore, the surface free energy was calculated using the van Oss model with three types of liquids, namely DI water, glycerol, and diiodomethane, as probes for the surface free energy calculation. Optical transmittance and bandgap energy analysis and calculations were performed using a UV–Vis spectrophotometer (Lambda 35, Perkin–Elmer). Finally, the electrical properties of the films were measured using a Hall measurement system (HMS-3000, ECOPIA) based on the van der Pauw method.

3 Results and Discussion

3.1 Etching Characteristics

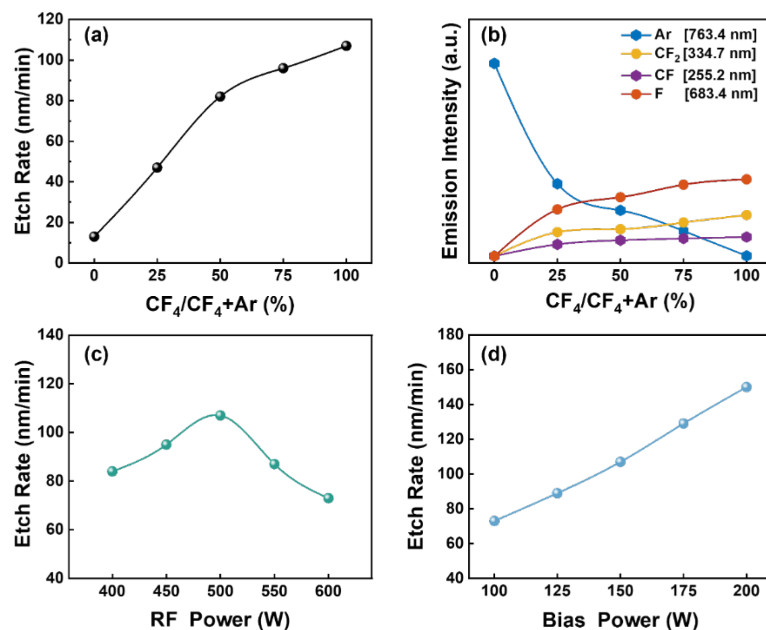

Fig. 1 Etching characteristics of fluorine-doped tin oxide (FTO) films in a CF_4-based plasma system. (**a**) Etching rate depending on the gas mixing ratio of CF_4/Ar. (**b**) The emission intensity of ions and radicals obtained via optical emission spectroscopy (OES) analysis during the etching process. Etching rates based on the (**c**) radio frequency (RF) and (**d**) bias powers

Fig. 1(a) depicts the influence of the CF_4/(CF_4/Ar) gas flow rate on the etching rate of the FTO film at an RF power of 500 W, a bias power of 150 W, and working pressure of 15 mTorr. The etching rate was extremely low (13 nm/min) before adding the CF_4 gas. As the concentration of the CF_4 gas in the CF_4/Ar plasma increased from 25 to 100%, the etching rate of the FTO thin films increased from 47 nm/min to a maximum value of 107 nm/min. This indicates that the CF_4 gas content is crucial for promoting chemical reactions on the surface of FTO thin films. This can be attributed to the increase in CF_X and F radicals, which enhances the rate of the chemical reactions with tin and oxygen. The comparison of etching rates under pure Ar and CF_4 plasmas indicates that the chemical etching was more effective than the physical sputtering etch pathway in the case of FTO thin films.

OES analysis is a technique used for measuring species and radical densities based on the intensity of the emission wavelength and the electron distribution function. Therefore, we used OES to determine the correlation between the relative changes in the emission intensity of the active species in the CF_4-based plasma and the etching rate behavior of the FTO films. The dissociated species were identified as Ar (763.4 nm), CF_2 (334.7 nm), CF (255.2 nm), and F (683.4 nm) [28], as depicted in Fig. 1(b). The emission intensities of CF_2, CF, and F radicals acting on the chemical etching process enhanced significantly when 25 sccm of CF_4 gas was added. Simultaneously, the proportion of Ar ions that determines the physical etching in the plasma reduced significantly. The emission intensities of the CF_2, CF, and F radicals from the CF_4/Ar plasma continued to increase as the CF_4 gas flux increased. This implies that the overall chemical reaction potential increases with the increase in the quantity of chemically active radicals in the plasma, rendering the chemically reactive etching of the FTO film more favorable. Consequently, the increase in the number of active species in the plasma owing to the increase in the CF_4 flux exhibits a positive correlation with the etching rate.

Etching characteristics are affected by the type of plasma gas, density of the plasma, and bombardment energy of the ions. To understand the etching characteristics, we observed the etching rate caused by changes in the RF and bias powers under pure CF_4 plasma conditions. As depicted in Fig. 1(c), the etching rate initially increased and then decreased as the RF power increased. An increase in RF power increases the density of reactive radicals and ions in the plasma, thereby increasing the etching rate [29]. The decrease in etching rate can be attributed to the excessive RF power, which reduces the sheath voltage on the lower electrode, weakens the physical sputtering energy, and results in the accumulation of etching by-products on the surface. Fig. 1(d) indicates that the etching rate increased based on the increase in the bias power. This result can be attributed to the increase in the ion bombardment energy caused by the increased bias power, rendering it easier to break the bonding of by-products on the film surface, which in turn increases the etching rate [30].

3.2 Structural Characterization

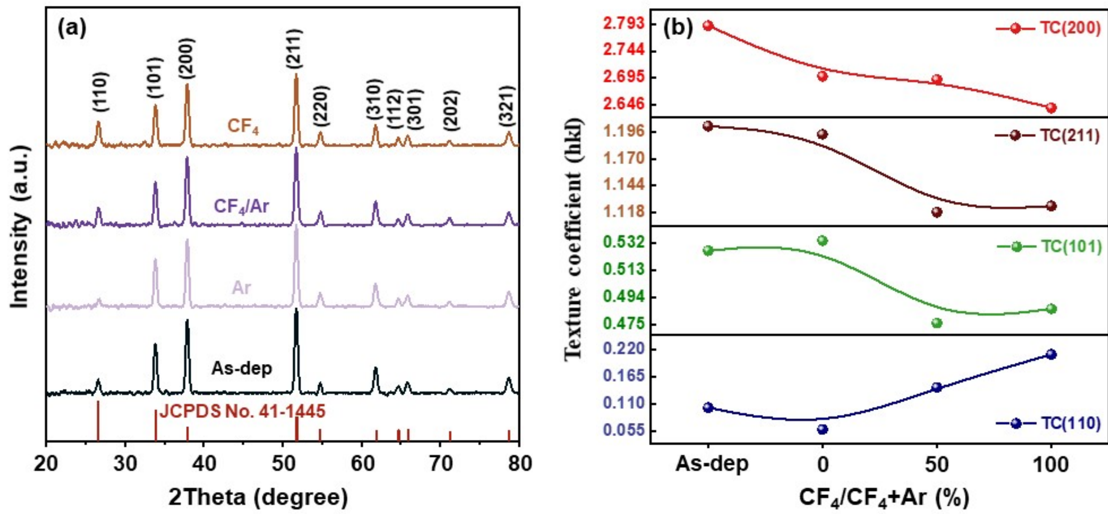

Fig. 2 (**a**) X-ray diffraction (XRD) patterns of fluorine-doped tin oxide (FTO) films under different etching conditions. (**b**) Variations of (110), (101), (211), and (200) texture coefficients of FTO films before and after etching

During the etching process, the reaction of energetic particles in the plasma causes unavoidable damage to its crystal structure. Fig. 2(a) illustrates the crystallographic changes in FTO films etched under different conditions, which were analyzed using XRD. The as-deposited (as-dep) and etched samples exhibit similar XRD patterns, and all the characteristic diffraction peaks corresponding to the tetragonal rutile structure of SnO_2 concur with those indicated in the Joint Committee on Powder Diffraction Standards (JCPDS) card number 41-1445. Secondary structure peaks, such as the SnO and SnF_2 compounds, were not identified in the graph. Additionally, the primary diffraction peaks of all samples were observed in the (101), (200), and (211) planes, indicating that the growth of the films was predominantly along these directions. The variation in the (110) peak with a relatively weak intensity can be associated with the etching conditions.

To quantify the variation in peak intensity under etching conditions, the texture coefficient (TC) for each plane was calculated using Eq. (1) [31].

$$TC(h\,k\,l) = \frac{\frac{I(h\,k\,l)}{I_0(h\,k\,l)}}{(\frac{1}{N})\sum_n \frac{I(h\,k\,l)}{I_0(h\,k\,l)}} \qquad (1)$$

where $I\ (h\ k\ l)$ denotes the measured intensity, $I_0\ (h\ k\ l)$ indicates the corresponding standard intensity obtained from the JCPDS card, and N represents the diffraction number; Fig. 2(b) depicts the corresponding results. The value of TC along the (200) plane is relatively high for all samples in comparison with other planes, indicating that the (200) plane is the preferred orientation for this film. Additionally, the preferred orientation of the FTO films remained unchanged after plasma etching. The

values of TC(101), TC(200), and TC(211) of the etched sample decreased under all etching conditions compared to those of the as-dep sample. The value of TC(110) changed slightly from 0.103 to 0.211 after the CF_4-based plasma etching, which can be inferred that (101), (200), and (211) planes were highly distributed on the surface during the growth process. [32, 33]. That is, the surface is removed by the etching process and the internal structure is exposed.

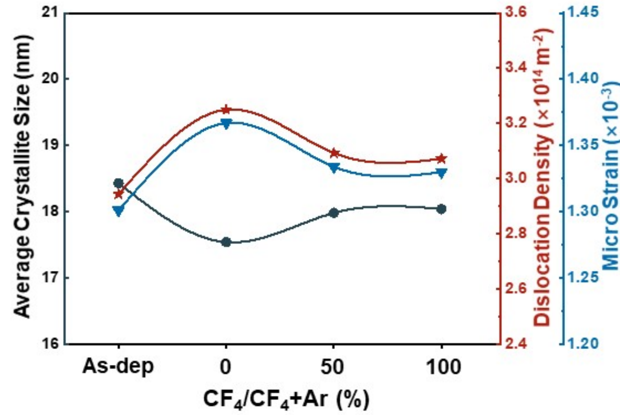

Fig. 3 Variations in crystallite size, dislocation density, and micro-strain along the (200) direction of the fluorine-doped tin oxide (FTO) films before and after etching

We calculated the lattice constants (a, c, and volume (V)) of the tetragonal structure of the FTO films before and after etching based on the lattice spacing of the (110) and (101) planes using Eq. (2) [34].

$$\frac{1}{d_{hkl}^2} = \frac{h^2+k^2}{a^2} + \frac{l^2}{c^2} \tag{2}$$

where *h, k,* and *l* denote the Miller indices, and *d* indicates the plane spacing. The lattice parameters tend to decrease after Ar plasma treatment and increase after CF_4-based plasma treatment, as presented in Table S1. This variation in lattice parameters can be associated with defects and lattice disorder, which changes the structural properties, such as micro-strain and dislocation [35, 36]. Therefore, the average crystalline size (D), dislocation density (δ), and micro-strain (ε) of the samples were determined using the following equations [37]:

$$D = \frac{K\lambda}{\beta \cos\theta} \tag{3}$$

$$\delta = \frac{1}{D^2} \tag{4}$$

$$\varepsilon = \beta \cot\theta - \frac{\lambda}{D \sin\theta} \tag{5}$$

where K denotes the Scherrer constant (0.9), λ indicates the X-ray wavelength (0.154 nm), β represents the full-width at half-maximum, and θ denotes the Bragg angle. Fig. 3 and Table S2 present the calculated parameter values under different etching conditions. The crystalline size decreased and

crystal defects, such as micro-strain and dislocation density, increased in all etched films compared to the as-dep FTO film. The most significant change was observed in the sample etched under the Ar plasma treatment. This can be attributed to the Ar ion bombardment increasing the number of structural oxygen vacancies, causing charge imbalance and lattice distortion. In CF_4-based plasmas, the generated F ions rapidly occupy oxygen vacancies that are caused by ion bombardment, alleviating charge imbalance and the gradual reduction of crystal defects by adjusting the lattice order [38]. This result indicates that plasma etching can increase defects or implant impurities in thin films.

3.3 XPS Analysis and Etching Mechanism

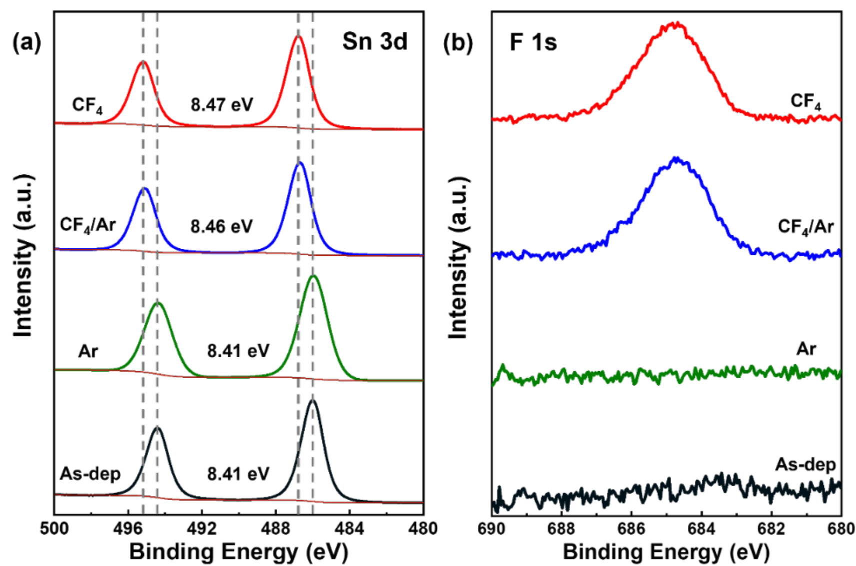

Fig. 4 High-resolution X-ray photoelectron spectroscopy (XPS) spectra of fluorine-doped tin oxide (FTO) films before and after the CF_4-based plasma etching. (**a**) Sn 3d and (**b**) F 1s

XPS analysis provides the compositional changes and residues on the film surface after the etching process, which can aid the evaluation of the etching mechanism. Therefore, we performed XPS analysis of the FTO films before and after the CF_4-based plasma etching. All the binding energies were corrected using the C 1s of 284.5 eV as a reference. Fig. 4(a) depicts the spectra of Sn 3d for the FTO thin films before and after etching. The Sn 3d spectra exhibit a doublet comprising two peaks at 486.41 eV (Sn $3d_{3/2}$) and 494.82 eV (Sn $3d_{5/2}$), which are caused by spin-orbit splitting [39]. The spin-orbit splitting of Sn 3d before etching is 8.41 eV, which corresponds to the chemical state of Sn^{4+} in SnO_2 [40, 41]. The spin-orbit splitting of Sn 3d increases to 8.47 eV after the CF_4-based plasma etching. Therefore, it can be inferred that Sn^{4+} combines with other atoms during the etching process, which is closely associated with the chemical reaction of the F radicals in the oxygen sites of the SnO_2 lattice. To confirm the small

shift of the Sn 3d peak, we observed the F 1s core-level spectra of the samples (Fig. 4(b)). As the doping content of fluorine in the as-dep sample was extremely low (only 0.62%), no binding energy was detected for F. In the samples etched under the CF_4-based plasma treatment, the chemical bond between tin and fluorine (Sn−F) was observed at 684.97 eV [42, 43]. These results indicate that surface oxygen atoms can be easily substituted by F atoms upon exposure to CF_4-based plasma because Sn binds stably to F than O; the Gibbs free energy change (ΔG) for SnO fluorination is negative [44, 45].

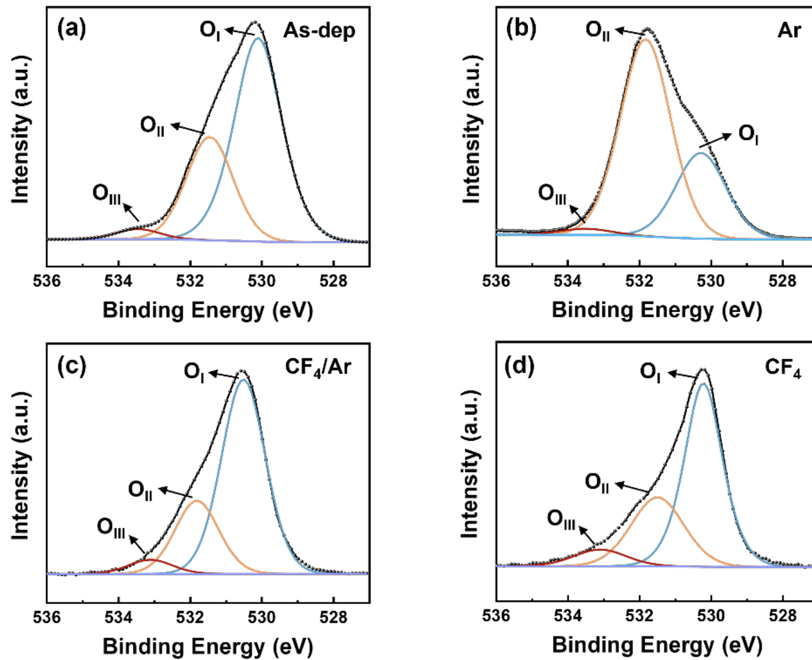

Fig. 5 O 1s X-ray photoelectron spectroscopy (XPS) narrow scans of the fluorine-doped tin oxide (FTO) films after CF_4-based plasma etching. (**a**) As-dep, (**b**) Ar, (**c**) CF_4/Ar, and (**d**) CF_4 samples

Fig. 5 depicts the narrow-scan spectra of the O 1s region on the surface of the FTO films. To investigate the composition combined with oxygen, each spectrum was deconvoluted into three peaks. The low binding peak at 530.1 ± 0.1 eV was attributed to the O^{2-} state of oxygen in the SnO_2 lattice, referred to as O_I [46]. The middle binding peak at 531.8 ± 0.1 eV was associated with oxygen vacancies in the oxygen-deficient regions, referred to as O_{II} [47]. Finally, the high binding peak at 533.3 ± 0.1 eV was assigned to hydroxyl (OH) on the surface of the FTO films, referred to as O_{III} [48]. The comparison of Figs. 5(a), 5(c), and 5(d) indicates that the intensity of the O_I peak was reduced after CF_4/Ar and CF_4 plasma treatments. This trend implies that the bond between Sn and O atoms is broken during etching, which enhances the reaction of Sn atoms with F radicals and that of O atoms with CF_2 and CF radicals [49]. Additionally, the high similarity between the atomic radii of F and O facilitates F radicals to occupy the oxygen vacancies during the etching process, reducing the intensity of the O_{II} peak [38]. By contrast, the intensity of the O_{III} peak increased, which can be attributed to the excellent electronegativity of the F ions. When F ions are bonded on the surface, they attract nearby hydrogen atoms and dangling oxygen

bonds, resulting in the formation of intermolecular F-HO hydrogen bonds [50]. Conversely, the sample etched under Ar plasma treatment indicates that the intensity of the O_I peak decreased, whereas the intensity of the O_{II} peak increased (Fig. 5(b)). This indicates that the ion bombardment effect in Ar plasma breaks the metal-oxide bonds, resulting in the escape of oxygen atoms from the SnO_2 lattice and the formation of oxygen vacancy defects [51]. This result is consistent with the XRD results and can explain the most severe crystal defects in the FTO films etched under Ar plasma treatment. In conclusion, the CF_4-based plasma etching breaks the Sn-O bonds in the FTO film, accompanied by the reaction of Sn and F radicals to generate Sn-F bonds on the surface. Furthermore, O is etched away by the CF_x radicals in the form of CFO and CO, as illustrated in Fig. 6.

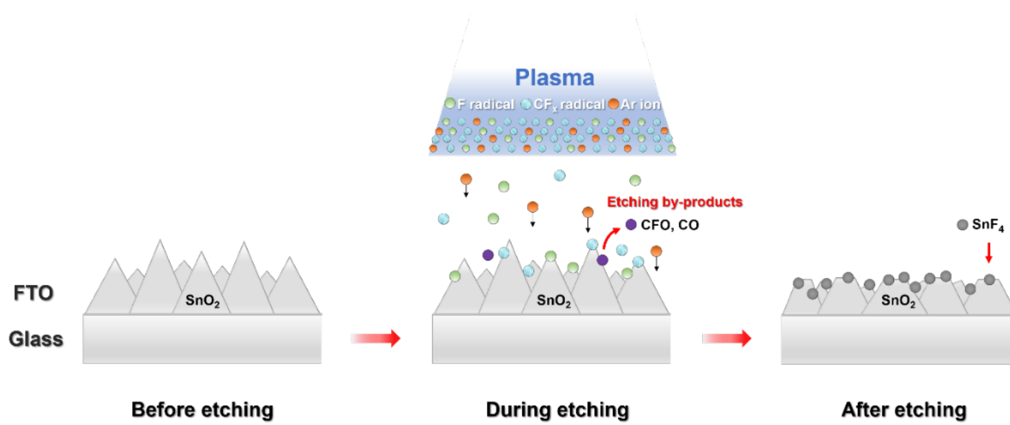

Fig. 6 Schematic of the etching mechanism of fluorine-doped tin oxide (FTO) films under CF_4-based plasma treatment

3.4 Surface Properties

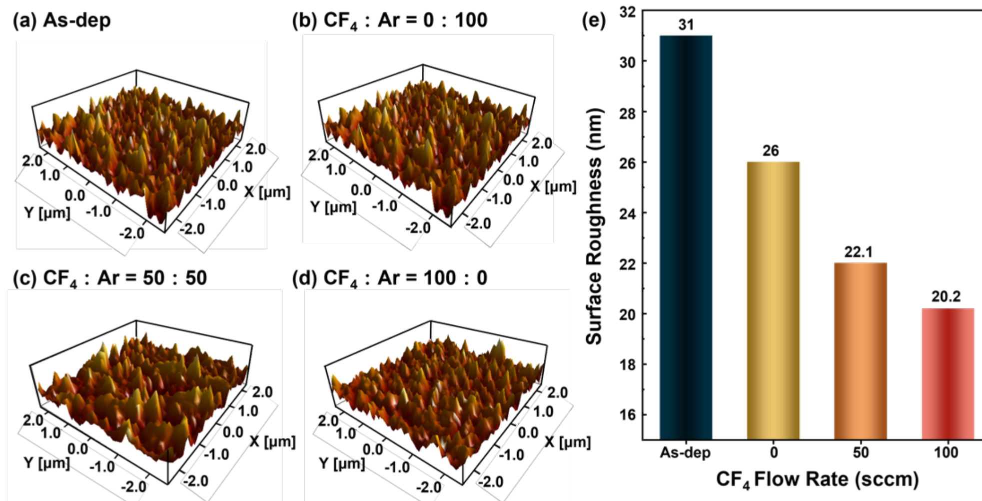

Fig. 7 Three-dimensional atomic force microscopy (AFM) images of fluorine-doped tin oxide (FTO) films. (**a**) As-dep sample and (**b–d**) the etched FTO films based on the CF_4-based plasma etching. (**e**) Bar chart of the surface roughness based on the gas ratio

When a transparent conductive electrode is applied to photoelectric or electronic devices, the surface properties of the FTO film significantly affect the performance of the device [52, 53]. For example, for solar cells and photodetectors, a rough surface is more effective than a flat surface because it increases the surface area and increases light absorption [54, 55]. On the other hand, in the case of transparent capacitors or touch screens, a rough surface increases leakage current and deteriorates device performance [56, 57]. Therefore, the surface properties of the FTO films must be analyzed after etching. Fig. 7 illustrates the three-dimensional AFM images of the etched FTO films and bar charts of the variation in surface roughness with the CF_4/Ar gas ratio. The surface roughness was reduced to 26 nm after the Ar plasma etching. With the increase in the CF_4 gas ratio, the roughness of the FTO films was further reduced, and the surface roughness of the pure CF_4 gas was between 20.2 nm. This indicates that the surface roughness of the FTO film after etching was flattened owing to the physical sputtering effect and chemical reaction.

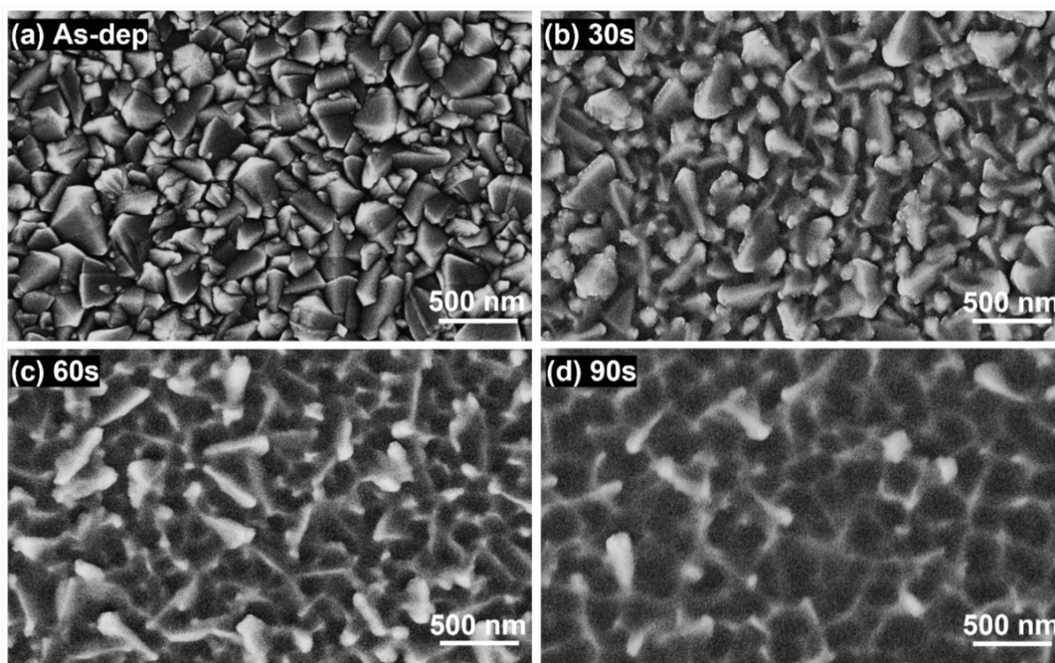

Fig. 8 Field emission scanning electron microscopy (FE-SEM) images of fluorine-doped tin oxide (FTO) films etched under CF_4 plasma treatment considering the process time. (**a**) As-dep sample and samples etched for (**b**) 30 s, (**c**) 60 s, and (**d**) 90 s

The FTO film surface was observed with respect to the etching time to obtain detailed information on the surface morphology during the etching process. Fig. 8(a) depicts the pyramidal crystals of different sizes that were distributed on the surface of the as-dep FTO film. The top sharp edges of the crystals were rounded at the beginning of the CF_4-based plasma etching process (Fig. 8(b)). As the etching time was increased, the protrusion on the film surface turned smoother. The accumulation of negative charges in the CF_4 plasma occurred at the tip of the pyramidal crystal, whereas the positively charged ions were

accelerated and concentrated in the part of the accumulated charge under the influence of the bias power supply; this resulted in a higher etching rate in the tip of the crystal than in other regions [58, 59]. Consequently, the surface of the FTO film progressively turned smoother with the increase in the etching time.

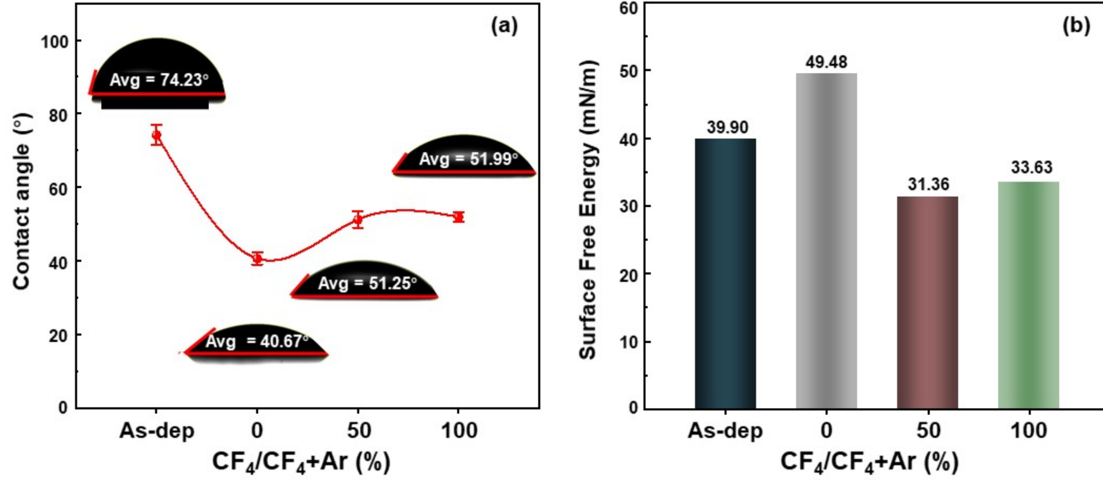

Fig. 9 (**a**) Contact angle change of fluorine-doped tin oxide (FTO) films in deionized water and the corresponding droplet photos before and after CF_4-based plasma etching. Error bars represent the standard deviation of eight replicates for each sample. (**b**) Calculated surface free energy value.

TCO films can be adapted to specific applications, such as printed electronic devices, gas, and biosensors by modifying the surface properties, including adhesion and surface free energy at the interface of the designed structure [60-62]. Fig. 9 depicts the contact angles of the FTO films before and after the CF_4-based plasma etching. The etched FTO films exhibited a significantly lower average contact angle (40.67–51.99 °) than the as-dep sample (74.23 °), which can be attributed to the improved surface roughness and the accumulation of highly electronegative F ions on the film surface after etching [63]. The surface free energy changes were calculated using the van Oss–Chaudhury–Good method (Eqs. (6)–(8)) based on the average contact angle data of a liquid triad comprising two polar liquids (DI water and glycerol) and one dispersive liquid (diiodomethane) [64].

$$\gamma_{LV}(1+cos\,\theta) = 2\left(\sqrt{\gamma_{SV}^{LW}\gamma_{LV}^{LW}} + \sqrt{\gamma_{SV}^{A}\gamma_{LV}^{B}} + \sqrt{\gamma_{SV}^{B}\gamma_{LV}^{A}}\right) \quad (6)$$

$$\gamma_{SV}^{AB} = 2\sqrt{\gamma_{SV}^{A}\gamma_{SV}^{B}} \quad (7)$$

$$\gamma_{SV}^{Total} = \gamma_{SV}^{LW} + \gamma_{SV}^{AB} \quad (8)$$

where *S, L,* and *V* represent solid, liquid, and vapor, respectively; γ_{SV}^{LW} denotes the Lifshitz–van der Waals surface free energy term, comprising dispersion, polar, and induction interactions; and γ_{SV}^{AB} indicates the acid–base interaction parameter of surface free energy, where *A* and *B* indicate the acid

and base, respectively. Tables S4 and S5 summarize the calculated values of the Lifshitz–van der Waals, acidic, and basic components of the surface free energy of the FTO samples. Fig. 9(b) illustrates the variations in the surface free energy before and after etching. All samples etched using the CF_4/Ar and CF_4 plasmas exhibited lower surface free energy than the as-dep sample (as-dep = 39.90 mN/m, CF_4/Ar = 31.36 mN/m, and CF_4 = 33.63 mN/m). The reduction in the surface free energy can be attributed to the halogen complex adsorbed on the surface after etching. A similar result was reported when the ITO film was treated with Cl_2 plasma [65]. This impacts the stacking process for subsequent device fabrication.

3.5 Physical Properties

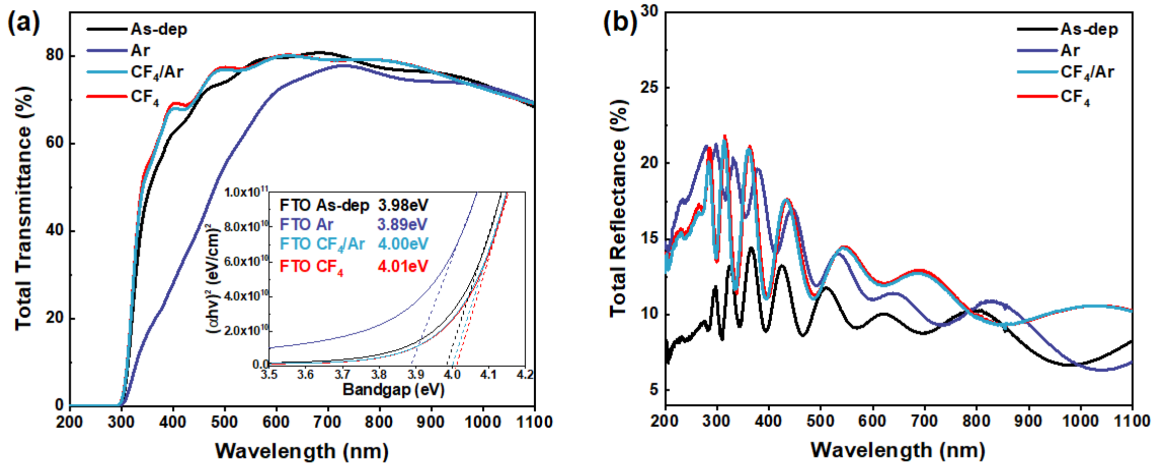

Fig. 10 (a) Total Transmittance and (b) reflectance spectrum of fluorine-doped tin oxide (FTO) films before and after the CF_4-based plasma etching. The inset of (a) depicts a plot of $(\alpha h\nu)^2$ versus $h\nu$ for estimating the bandgap

Fig. 10 depicts the changes in the optical properties of FTO films before and after etching. In the visible light region (λ = 360–700 nm), the average values of total transmittance were 73.5, 74.9, and 75.2% for the as-deposited film, film etched under CF_4/Ar plasma, and film etched under pure CF_4 plasma, respectively. On the other hand, the average values of total reflectance were 10.29, 13.68, and 13.49% for the as-deposited film, film etched under CF_4/Ar plasma, and film etched under pure CF_4 plasma, respectively. This can be attributed to the smoothened surface morphology, which alleviates photon scattering [66]. By contrast, pure Ar plasma etching significantly reduced the average transmittance (55.8%) and increased the reflectance (13.38%) of the FTO film. This is likely to cause extraction of Sn after physical sputtering during the etching process, resulting in a slight yellowing of the FTO film [67]. Based on the transmittance data, the bandgap of the FTO films was calculated using the Tauc method (Eq. 9) [68].

$$\alpha h\nu = A(h\nu - E_g)^n \tag{9}$$

where α denotes the absorption coefficient, A indicates the proportionality constant, E_g represents the optical bandgap of the material, and n = 1/2 for a direct allowed transition. The bandgap energy of the as-dep sample was 3.98 eV, and etching under CF_4-based plasma increased the bandgap energy by 0.02 eV (CF_4/Ar) and 0.03 eV (CF_4). The bandgap of tin oxide is based on the excitation of electrons from the valence band to the conduction band. The increased carrier concentration after etching promotes the lowest energy level in the conduction band from the empty to the filled state, which pushes the Fermi level to higher energies (the Moss–Burstein effect) [69, 70]. Therefore, the bandgap of the FTO film was widened after the CF_4-based plasma treatment.

Table 1 Summary of electrical properties and average transmittance variation of FTO films under the CF_4-based plasma etching

	As-dep	Ar	CF_4/Ar	CF_4
Hall mobility ($cm^2/(V\cdot s)$)	39.4	38.4	38.9	38.4
Carrier concentration (cm^{-3})	3.38×10^{20}	3.52×10^{20}	3.69×10^{20}	3.86×10^{20}
Resistivity ($\Omega\cdot cm$)	4.70×10^{-4}	4.62×10^{-4}	4.35×10^{-4}	4.21×10^{-4}
Sheet resistance (Ω/sq)	7.83	7.87	8.40	9.39
Transmittance (%)	73.5	55.8	74.9	75.2

Electrical properties, such as resistivity(ρ), carrier concentration(n), Hall mobility (μ), and sheet resistance are crucial in determining the applicability of TCO materials [71]. Therefore, we confirmed the variation in the electrical properties of FTO films under different etching conditions using the Hall-effect measurements. Five samples were prepared and measured for each condition; Table 1 lists the average results. The carrier concentration of the FTO films increased after etching. In the case of samples etched under Ar plasma treatment, the induction of oxygen vacancies in the SnO_2 structure led to an increase in carrier concentration [72]. In the case of samples etched under the CF_4-based plasma treatment, the substitution of O_2 ions by F ions added a free electron to the SnO_2 structure [73]. Additionally, the mobility of all etched samples decreased slightly from 39.4 $cm^2/(V\cdot s)$ to 38.4 $cm^2/(V\cdot s)$, which can be attributed to the intergranular boundary scattering caused by the crystallite size. In terms of resistivity, the increase in carrier concentration compensated for the deterioration in mobility. Therefore, the FTO film etched under the CF_4-based plasma treatment exhibited the lowest resistance of 4.21×10^{-4} $\Omega\cdot cm$. Conversely, the sheet resistance values of etched FTO films all slightly increased.

4 Conclusions

This study analyzed the etching characteristics and surface properties of FTO films in an HDP system under CF_4-based plasma treatment. The etching rate increased with the increase in the CF_4 gas flux, and the maximum etching rate was 107 nm/min in the case of pure CF_4 plasma. Additionally, the etching

characteristics of the FTO film can be changed by varying the process parameters, such as the RF and bias powers. Plasma etching increased the crystal defects of the FTO films, and the O and Sn components in the FTO films combined with F and CF_X radicals changed the surface properties. The edges of the sharp crystals on the surface of the FTO film turned smooth owing to the CF_4-based plasma etching, which contributed to the smoothening of surface roughness and enhanced transmittance. The surface free energy of the FTO film changed significantly after the plasma etching. Furthermore, the increased carrier concentration caused by the change in the FTO surface after the etching widened the bandgap to 4.01 eV and reduced the resistance to 4.21×10^{-4} Ω·cm. These results can potentially improve the performance of optoelectronic devices via plasma processing and facilitate the implementation of FTO films for micro-patterning in various optical device applications.

Declarations

Author contributions

Wenhui Yu: Conceptualization, Methodology, Investigation, Data Curation, Visualization, Writing - original draft; **Jeong Geun Lee:** Investigation, Data Curation; **Young-Hee Joo:** Methodology, Visualization; **Bo Hou:** Data Curation, Writing - review and editing; **Doo-Seung Um:** Conceptualization, Validation, Resources, Visualization, Writing - review and editing, Supervision, Funding acquisition; **Chang-Il Kim:** Conceptualization, Writing - review and editing, Supervision, Project administration, Funding acquisition.

Funding

This research was supported by the Chung-Ang University Young Scientist Scholarship (2020) and the National Research Foundation (NRF) of Korea (2020R1G1A1102692).

Data availability

All data supporting the findings of this study are included in the article (and any supplementary files).

Conflict of interest

The authors declare no conflicts of interest.

References

1. J. Lee, P. Lee, H. Lee, D. Lee, S. S. Lee and S. H. Ko, Nanoscale **4** (20), 6408-6414 (2012).
2. S.-H. Park, S.-M. Lee, E.-H. Ko, T.-H. Kim, Y.-C. Nah, S.-J. Lee, J. H. Lee and H.-K. Kim, Sci. Rep. **6** (1), 1-12 (2016).
3. B. Li, B. Hou and G. A. Amaratunga, InfoMat **3** (5), 445-459 (2021).
4. B. Li, M. Lu, J. Feng, J. Zhang, P. M. Smowton, J. I. Sohn, I.-K. Park, H. Zhong and B. Hou, J. Mater. Chem. C **8** (31), 10676-10695 (2020).
5. T. Minami, Semicond. Sci. Technol. **20** (4), S35 (2005).
6. H. Kim, a. C. Gilmore, A. Pique, J. Horwitz, H. Mattoussi, H. Murata, Z. Kafafi and D. Chrisey, J. Appl. Phys. **86** (11), 6451-6461 (1999).
7. T. Minami, H. Sato, H. Nanto and S. Takata, Thin Solid Films **176** (2), 277-282 (1989).
8. A. Kumar and C. Zhou, ACS nano **4** (1), 11-14 (2010).
9. D. Cheng, M. Zhang, J. Chen, C. Yang, X. Zeng and D. Cao, J. Phys. Chem. C **118** (4), 2037-2043 (2014).
10. Y. Liu, Y. Li and H. Zeng, J. Nanomater. **2013** (2013).
11. M. Zhang, S. Fang, A. A. Zakhidov, S. B. Lee, A. E. Aliev, C. D. Williams, K. R. Atkinson and R. H. Baughman, Science **309** (5738), 1215-1219 (2005).
12. V. C. Tung, L.-M. Chen, M. J. Allen, J. K. Wassei, K. Nelson, R. B. Kaner and Y. Yang, Nano Lett. **9** (5), 1949-1955 (2009).
13. S. De, T. M. Higgins, P. E. Lyons, E. M. Doherty, P. N. Nirmalraj, W. J. Blau, J. J. Boland and J. N. Coleman, ACS nano **3** (7), 1767-1774 (2009).
14. J. Hong, B.-S. Kim, B. Hou, S. Pak, T. Kim, A.-R. Jang, Y. Cho, S. Lee, G.-H. An and J. E. Jang, ACS Appl. Mater. Interfaces **13** (3), 4244-4252 (2021).
15. Q. Qiao, J. Beck, R. Lumpkin, J. Pretko and J. T. Mcleskey Jr, Sol. Energy Mater. Sol. Cells **90** (7-8), 1034-1040 (2006).
16. V. Kotok, V. Malyshev, V. Solovov and V. Kovalenko, ECS J. Solid State Sci. Technol. **6** (12), 772 (2017).
17. S. Triana and R. Suryana, Journal of Physics: Conference Series **776**, 012005 (2016).
18. J.-W. Bae, B.-R. Koo, H.-R. An and H.-J. Ahn, Ceram. Int. **41** (10), 14668-14673 (2015).
19. S. Koiry, P. Jha, P. Veerender, C. Sridevi, A. Debnath, A. Chauhan, K. Muthe and S. Gadkari, J. Electrochem. Soc. **164** (2), E1 (2016).
20. Y.-l. Wang, B.-j. Li, S.-s. Li, H. Li, L.-j. Huang and N.-f. Ren, Opt. Laser Technol. **116**, 162-170 (2019).
21. H. Yang, D. Fu, M. Jiang, J. Duan, F. Zhang, X. Zeng and U. Bach, Thin Solid Films **531**, 519-524 (2013).

22. S.-F. Tseng, W.-T. Hsiao, D. Chiang, C.-K. Chung and J.-L. A. Yeh, Opt. Lasers Eng. **52**, 212-217 (2014).
23. F. I. Chowdhury, T. Blaine and A. B. Gougam, Energy Procedia **42**, 660-669 (2013).
24. N. Chantarat, S.-H. Hsu, C.-C. Lin, M.-C. Chiang and S.-Y. Chen, J. Mater. Chem. **22** (16), 8005-8012 (2012).
25. P. Tang, C. Liu, J. Zhang, L. Wu, W. Li, L. Feng, G. Zeng and W. Wang, Appl. Surf. Sci. **436**, 134-140 (2018).
26. C.-H. Huang, Y.-J. Lu, Y.-C. Pan, H.-L. Liu, J.-Y. Chang, J.-L. Sie, D.G. Pijanowska, C.-M. Yang, Nanomaterials **12**, 1925 (2022).
27. Y.-H. Joo, D.-S. Um and C.-I. Kim, Mater. Res. Express **8** (12), 126402 (2021).
28. R. Wang, C. Zhang, X. Liu, Q. Xie, P. Yan and T. Shao, Appl. Surf. Sci. **328**, 509-515 (2015).
29. G. Das, S. Bose, J. R. Sharma, S. Mukhopadhyay and A. K. Barua, J. Mater. Sci: Mater. Electron. **29** (8), 6206-6214 (2018).
30. L. Zhang, Y.-H. Joo, D.-S. Um and C.-I. Kim, Mater. Res. Express **7** (10), 106301 (2020).
31. Y. Wang, W. Tang and L. Zhang, J. Mater. Sci. Technol. **31** (2), 175-181 (2015).
32. A. H. Omran Alkhayatt and S. K. Hussian, Mater. Lett. **155**, 109-113 (2015).
33. N. Haddad, Z. Ben Ayadi, H. Mahdhi and K. Djessas, J. Mater. Sci.: Mater. Electron. **28** (20), 15457-15465 (2017).
34. K. D. A. Kumar, S. Valanarasu, K. Jeyadheepan, H.-S. Kim and D. Vikraman, J. Mater. Sci.: Mater. Electron. **29** (5), 3648-3656 (2017).
35. R. Thomas, T. Mathavan, M. Jothirajan, H. Somaily, H. Zahran and I. Yahia, Opt. Mater. **99**, 109518 (2020).
36. S. Bansal, D. Pandya, S. C. Kashyap and D. Haranath, J. Alloy. Compd. **583**, 186-190 (2014).
37. G. Turgut, E. Sonmez, S. Aydın, R. Dilber and U. Turgut, Ceram. Int. **40** (8), 12891-12898 (2014).
38. X. Wang, X. Wang, Q. Di, H. Zhao, B. Liang and J. Yang, Materials **10** (12), 1398 (2017).
39. D. Deepu, C. S. Kartha and K. Vijayakumar, J. Anal. Appl. Pyrolysis **121**, 24-28 (2016).
40. F. El Akkad and T. A. Paulose, Appl. Surf. Sci. **295**, 8-17 (2014).
41. F. Gu, H. Wang, D. Han and Z. Wang, Sens. Actuators B-Chem. **245**, 1023-1031 (2017).
42. B. R. Koo, D. H. Oh, D. H. Riu and H. J. Ahn, ACS Appl. Mater. Interfaces **9** (51), 44584-44592 (2017).
43. V. Kumar, A. Govind and R. Nagarajan, Inorg. Chem. **50** (12), 5637-5645 (2011).
44. W. S. A. El-Yazeed, M. Eladl, A. I. Ahmed and A. A. Ibrahim, J. Sol-Gel Sci. Technol. **97** (1), 191-204 (2020).
45. M. Kanayama, T. Oku, T. Akiyama, Y. Kanamori, S. Seo, J. Takami, Y. Ohnishi, Y. Ohtani and M. Murozono, Energy and Power Engineering **5** (02), 18-22 (2013).

46. F. M. Amanullah. K. J. Pratap, and V. H. Babu, Materials Science and Engineering **B52**, 93–98 (1998).
47. X. Wang, M. Xu, L. Liu, Y. Cui, H. Geng, H. Zhao, B. Liang and J. Yang, J. Mater. Sci.: Mater. Electron. **30** (17), 16110-16123 (2019).
48. A. R. Babar, S. S. Shinde, A. V. Moholkar, C. H. Bhosale, J. H. Kim and K. Y. Rajpure, J. Alloy. Compd. **509** (6), 3108-3115 (2011).
49. C.-Y. Lee, Y.-H. Joo, M. P. Kim, D.-S. Um and C.-I. Kim, Coatings **11** (8) (2021).
50. E. Polydorou, A. Zeniou, D. Tsikritzis, A. Soultati, I. Sakellis, S. Gardelis, T. A. Papadopoulos, J. Briscoe, L. C. Palilis, S. Kennou, E. Gogolides, P. Argitis, D. Davazoglou and M. Vasilopoulou, J. Mater. Chem. A **4** (30), 11844-11858 (2016).
51. H. Park, D. Kim, E.-C. Cho, S. Q. Hussain, J. Park, D. Lim, S. Kim, S. Dutta, M. Kumar and Y. Kim, Curr. Appl. Phys. **20** (1), 219-225 (2020).
52. W. Cao, J. Li, H. Chen and J. Xue, J. Photonics Energy **4** (1), 040990 (2014).
53. A.H. Ali, Z. Hassan and A. Shuhaimi, Appl. Surf. Sci. **443**, 544-547 (2018).
54. M. Jost, E. Kohnen, A. B. Morales-Vilches, B. Lipovsek, K. Jager, B. Macco, A. Al-Ashouri, J. Krc, L. Korte, B. Rech, R. Schlatmann, M. Topic, B. Stannowski and S. Albrecht, Energy Environ. Sci. **11**, 3511-3523 (2018).
55. D. S. Um, S. Lim, Y. Lee, H. Lee, H. J. Kim, W. C. Yen, Y. L. Chueh and H. Ko, ACS Nano **8** (3), 3080-3087 (2014)
56. C. J. Xian and S. G. Yoon, J. Electrochem. Soc. **156** (11), G180-G183 (2009)
57. H. S. Wang, T. H. Im, Y. B. Kim, S. H. Sung, S. Min, S. H. Park, H. E. Lee, C. K. Jeong, J. H. Park and K. J. Lee, APL Mater. **9**, 061112 (2021)
58. V. Ishchuk, B. E. Volland, M. Hauguth, M. Cooke and I. W. Rangelow, J. Appl. Phys. **112** (8) (2012).
59. K.-T. Lee and S.-Y. Lu, RSC Adv. **3** (23) (2013).
60. S. Vunnam, K. Ankireddy, J. Kellar and W. Cross, Thin Solid Films **531**, 294-301 (2013).
61. G. Lee, E. Park, V.-T. Nguyen, S. Heo, N.-A. Nguyen, L. L. Larina, I. Yoon and H.-S. Choi, Appl. Surf. Sci. **551** (2021).
62. S. Ozbay, N. Erdogan, F. Erden, M. Ekmekcioglu, B. Rakop, M. Ozdemir, G. Aygun and L. Ozyuzer, Appl. Surf. Sci. **567** (2021).
63. J. Wang, Y. Wu, Y. Cao, G. Li, and Y. Liao, Colloid Polym. Sci. **298** (8), 1107-1112 (2020).
64. C. J. van Oss, J. Adhes. Sci. Technol. **16** (6), 669-677 (2002).
65. S.-G. Jung, K. B. Choi, C. H. Park, Y. S. Shim, C. H. Park, Y. W. Park and B.-K. Ju, Opt. Mater. **93**, 51-57 (2019).
66. M.-H. Jo, B.-R. Koo and H.-J. Ahn, Ceram. Int. **46** (16), 25066-25072 (2020).
67. K. N. Manjunatha and S. Paul, Appl. Surf. Sci. **424**, 316-323 (2017).

68. P. Makula, M. Pacia and W. Macyk, J. Phys. Chem. Lett. **9** (23), 6814-6817 (2018).
69. Z. Banyamin, P. Kelly, G. West and J. Boardman, Coatings **4** (4), 732-746 (2014).
70. M. Batzill and U. Diebold, Prog. Surf. Sci. **79** (2-4), 47-154 (2005).
71. H. Heffner, M. Soldera, and A. F. Lasagni, Adv. Eng. Mater **2022**, 2200266 (2022)
72. M. Fantini and I. Torriani, Thin solid films **138** (2), 255-265 (1986).
73. K. Rajshekar, H.-H. Hsu, K. U. M. Kumar, P. Sathyanarayanan, V. Velmurugan, C.-H. Cheng and D. Kannadassan, IEEE Trans. Electron Devices **66** (3), 1314-1321 (2019).